O'Donnell, M. P., Stacey, J. P., Chenchiah, I. V., & Pirrera, A. (2019). Multiscale tailoring of helical lattice systems for bespoke thermoelasticity. *Journal of the Mechanics and Physics of Solids*, *133*, Article 103704. https://doi.org/10.1016/j.jmps.2019.103704

Peer reviewed version

License (if available):
CC BY-NC-ND

Link to published version (if available):
10.1016/j.jmps.2019.103704

Link to publication record on the Bristol Research Portal
PDF-document

This is the author accepted manuscript (AAM). The final published version (version of record) is available online via Elsevier Ltd at https://www.sciencedirect.com/science/article/pii/S0022509619305538 . Please refer to any applicable terms of use of the publisher.

University of Bristol – Bristol Research Portal

General rights

This document is made available in accordance with publisher policies. Please cite only the published version using the reference above. Full terms of use are available: http://www.bristol.ac.uk/red/research-policy/pure/user-guides/brp-terms/

Multiscale Tailoring of Helical Lattice Systems for Bespoke Thermoelasticity

Matthew P. O'Donnell[a,*], Jonathan P. Stacey[a], Isaac V. Chenchiah[b], Alberto Pirrera[a]

[a]*Bristol Composites Institute (ACCIS), University of Bristol, Queen's Building, Bristol UK, BS8 1TR*
[b]*School of Mathematics, University of Bristol, University Walk, Bristol UK, BS8 1TW*

Abstract

(Meta-)Materials, e.g. functional or architectured materials that change shape in response to external stimuli, often do so by exploiting solid-solid phase transitions or concerted elastic deformations. For the resulting system to be effective the (meta-)material needs to have desirable and tunable properties at length scales sufficiently small that desirable continuum behaviour of the resulting component is obtained. Developing such (meta-)materials has proven to be an endeavour which requires considerable expertise in science, engineering and mathematics. Here, we pursue an alternative approach where the design for functionality is integrated across multiple length scales in the system. We demonstrate this approach by designing and prototyping helical lattices that act as one-dimensional thermoelastic materials with unusual properties such as negative thermal expansivity—with magnitude far exceeding the most extreme values reported in the literature—and zero-hysteresis shape memory. Our strategy is independent of characteristic length scale, allowing us to design behaviour across a range of dimensions.

Keywords: Nonlinear Elasticity, Thermoelastic Materials, Composites, Anisotropy, Meta-Materials, Architected-Materials

---

1. Introduction

Structures possessing transformative properties, often derived from phase-changing materials, can adapt to the environment or to changing operating conditions without requiring complex actuation mechanisms. The potential advantages offered by transformative materials have led to significant development efforts—shape memory alloys (SMAs) are a well-known example [1]. In particular, a considerable part of these efforts has been dedicated to the tuning of the thermal properties of materials for bespoke adaptivity [2–5]. Nevertheless, at material level, the resulting performance is often inerently limited by, e.g., small strains, large temperature hysteresis and low stiffness.

Instead of attempting to tailor material properties to obtain desired macroscopic responses, our design for structural-level functionality is integrated across length scales. By exploiting the interplay between

---

[*] Corresponding Author: Matt.ODonnell@bristol.ac.uk

geometry, anisotropic stiffness and nonlinear elastic deformations in a helical lattice structure, we achieve adaptive macroscopic behaviours, while also significantly expanding the range of possible responses beyond what is attainable through material tailoring alone. By shifting complexity from material to structural design, we are reversing the prevailing materials science paradigm.

Specifically, we present a one-dimensional component, a helical lattice structure inspired by the virus Bacteriophage T4 [6], which can:

- behave as SMAs at the structural length scale, *and*
- exhibit unusual thermal properties such as negative thermal expansivity.

The lattice is comprised of strips kinematically constrained to lie on the surface of a cylinder. Under thermal loading the anisotropic expansion of the strips, which induces curvature and twist in the strips themselves, interplays with this geometric constraint to enable a rich set of tunable constitutive behaviours. Such behaviours include:

- snap-through from a fully-coiled to fully-extended helix (or vice versa),
- transition from mono-stability to multi-stability at a designed critical temperature,
- smooth temperature-varying actuation, including negative thermal expansivity.

Similar exotic behaviour can be observed across length scales. For example, at the material level, crystalline lattices with negative thermal expansivities use geometric mechanisms analogous to those of the helical geometry proposed here [7]. More generally, functionality can be designed for from the nano-, to the architectured- and meta-material scale, all the way up to the macro-scale [8–17]. Tuneable thermal responses have been achieved by tailoring of meta-material lattices [18]. However, it is difficult to tune them while also maintaining desirable structural stiffness, because thermal and structural responses require design at different length scales. In contrast, our design for component-level functionality is integrated across length scales, since, by exploiting architecture, stress fields and material anisotropy synergistically, we blur the distinction between materials and structures.

We now proceed to identify the main features of the thermoelastic system presented herein.

2. Architectured Thermoelasticity

The helical lattice structure, illustrated in Figure 1, is effectively a one-dimensional nonlinear thermoelastic spring whose principal behaviour is expansion/contraction in the longitudinal direction. Depending on the choice of design parameters the system can transition from fully-coiled to fully-extended configurations. Longitudinal expansion(contraction) is accompanied by radial contraction(expansion). The lattice

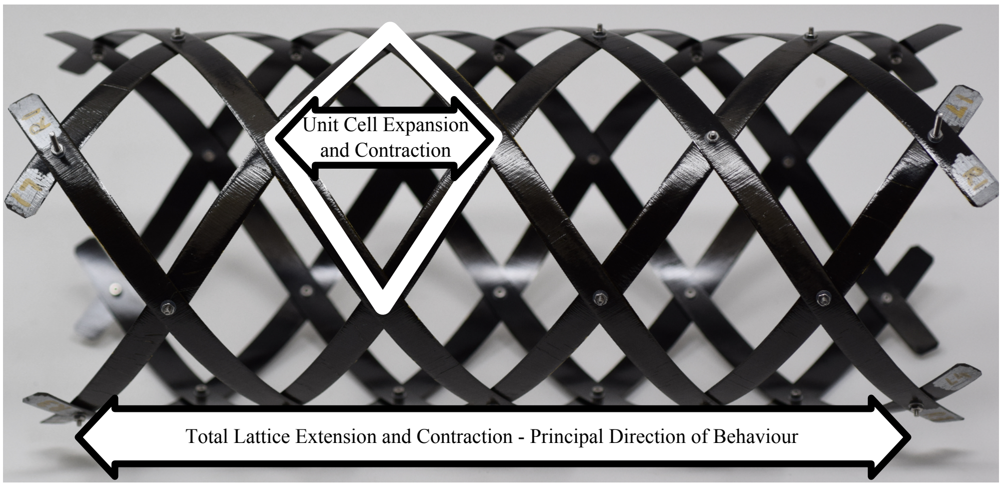
Unit Cell Expansion and Contraction
Total Lattice Extension and Contraction - Principal Direction of Behaviour

Figure 1: Prototype of an thermoelastic helical lattice. The principal behaviour occurs in the longitudinal direction. The global response can be captured by considering a representative unit cell.

is comprised of strips positioned in a helical arrangement constrained to lie on the surface of a cylinder. Strips of the same chirality possess a common pre-stress and anisotropic stiffness with regards to bending and twisting. The resulting nonlinear energy profile in response to extension/contraction drives the extreme responses observed in our analysis. The lattice shown is a macroscopic prototype, but the mechanics can be reproduced at various length scales.

The behaviour of the lattice can be accurately predicted through consideration of a representative unit cell. Consequently, we can tune the pre-stress, stiffness and geometry of the strips to produce a diverse range of extreme responses. The lattice response was shown to be robust, repeatable and tailorable [6].

An example of an extreme response is that of the prototype presented in Figure 1. Under heating the total lattice length contracts from 286 mm at 309 K to 193 mm at 408 K. This corresponds to an average coefficient of thermal expansion (CTE) of -3285×10^{-6} K^{-1}, which is over 1000 times larger than what is currently commercially available [19], and exceeds even the value of -515×10^{-6} K^{-1}, reported in the literature as extreme [20, 21].

We now proceed to outline how such bespoke thermoelasticity can be obtained and tailored by tuning the lattice energy landscape.

2.1. Lattice Geometry

The lattice is represented schematically in Figure 2 and comprises of N helices of each chirality and $4N$ unit cells. For simplicity, we consider only lattices with chiral symmetry, since then: (i) the unit cells are rhomboidal, (ii) the lattices elongate/contract without twisting, and (iii) the variable h (see Figure 2) characterises the system uniquely [6, 12]. The circumferential and longitudinal diagonals of the unit cell are

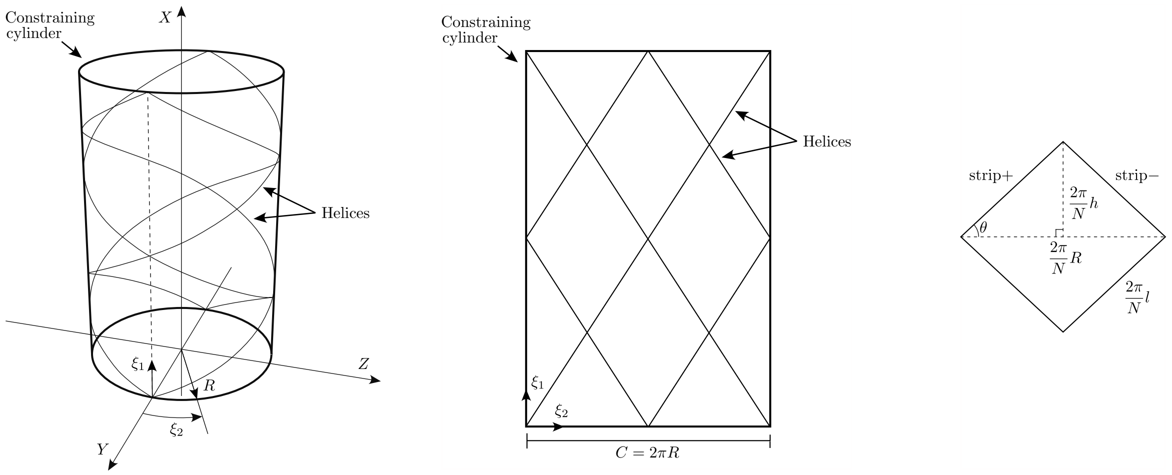
Constraining cylinder
X
Helices
Z
Y
ξ_1
ξ_2
R
Constraining cylinder
Helices
ξ_1
ξ_2
$C = 2\pi R$
strip+
strip−
θ
$\frac{2\pi}{N}h$
$\frac{2\pi}{N}R$
$\frac{2\pi}{N}l$

(a) A cylindrical lattice.

(b) Planar projection of lattice.

(c) Rhomboidal unit cell.

Figure 2: Sketch of (a) a helical lattice comprised of $N = 2$ strips on the surface of a constraining cylinder of radius R, (b) its planar representation, and (c) its unit cell.

$\frac{2\pi}{N}R$ and $\frac{4\pi}{N}h$, respectively, where R is the radius of the helices. It is then convenient to set the rhombus' side length to be $\frac{2\pi}{N}l$.

As the lattice deforms, we assume [6] that:

(i) all helices remain on a single cylinder (whose radius and length can change),

(ii) the helical strips are hinged where they overlap allowing scissoring motion only,

(iii) the change in length of the helical strips is negligible, and

(iv) the helical strips are sufficiently slender that the dominant contribution to the energy landscape arising from bending and twisting with respect to the strips' principal dimension.

Further on the kinematics, consider the '+' strip that passes through the origin in Figure 2(b). In the ξ-plane this strip has the parametrisation

$$s(\sin(\theta), \cos(\theta)),$$

where s is the arc-length parameter and θ is illustrated in Figure 2(c). From the assumptions above, this strips maps to the helix

$$s\sin(\theta)\hat{X} + RQ(\frac{\cos(\theta)}{R}s)\hat{Y}$$

in the (X, Y, Z) coordinate system used in Figure 2(a), where $Q(\phi)$ is a rotation with axis $\hat{X}$ through an angle ϕ. The tangent, normal and binormal can then be calculated to be

$$\begin{aligned} t(s) &= \sin(\theta)\hat{X} + \cos(\theta)Q(\frac{\cos(\theta)}{R}s)\hat{Z}, \\ n(s) &= -Q(\frac{\cos(\theta)}{R}s)\hat{Y}, \\ b(s) &= \cos(\theta)\hat{X} - \sin(\theta)Q(\frac{\cos(\theta)}{R}s)\hat{Z}, \end{aligned}$$

respectively. Finally, the curvature and torsion can be related to the geometry through

$$\kappa_x = t'(s)\cdot n(s) \quad = \frac{\cos^2(\theta)}{R} \quad = \frac{\sqrt{l^2-h^2}}{2l^2}, \tag{1a}$$

$$\kappa_{xy} = -b'(s)\cdot n(s) = \frac{\sin(\theta)\cos(\theta)}{R} = \frac{h}{2l^2}, \tag{1b}$$

respectively. These hold for the '$-$' strip as well, except that the sign of the torsion is reversed.

3. Total Potential Energy

3.1. Strain energy of the constituent material

Classical Laminate Theory (CLT), as applied to composites, provides a robust framework to capture the anisotropic, thermoelastic response of the structure under consideration [6]. The use of CLT is for notational convenience alone and does not imply that the system *must* be composed of composite strips. For example, anisotropy could be designed into the system by exploiting cross-sectional geometry or functionally-graded materials.

Let us consider a generic laminate, with the coordinate system (x, y, z) chosen such that z is the thickness direction. As is conventional, we assume that all layers are perfectly bonded to each other, and that the laminate's stiffness properties may be condensed to the mid-plane [22]. It follows that, for the kth layer, which is assumed to be orthotropic, stresses, $\boldsymbol{\sigma}^{(k)}$, and strains, $\boldsymbol{\epsilon} = \boldsymbol{\varepsilon} + z\boldsymbol{\kappa}$, are related in the laminate coordinates through the transformed stiffness matrix, $\bar{\boldsymbol{Q}}^{(k)}$, such that

$$\boldsymbol{\sigma}^{(k)} = \bar{\boldsymbol{Q}}^{(k)}\left(\boldsymbol{\epsilon} - \Delta T\boldsymbol{\alpha}^{(k)}\right), \tag{2}$$

where $\boldsymbol{\alpha}^{(k)} = [\alpha_{xx}^{(k)}, \alpha_{yy}^{(k)}, 2\alpha_{xy}^{(k)}]^\top$ is the vector coefficient of thermal expansion and the temperature change ΔT is $T - T_{\text{ref}}$, T being the current temperature and T_{ref} a reference temperature corresponding to the laminate's stress-free state.

Integrating (2) through the thickness, we obtain resultant forces and moments per unit width, $\mathbf{N}$ and $\mathbf{M}$, which are related to mid-plane strains, $\boldsymbol{\varepsilon}$, curvatures, $\boldsymbol{\kappa}$, and ΔT, through

$$\begin{bmatrix} \mathbf{N} \\ \mathbf{M} \end{bmatrix} = \begin{bmatrix} \mathbf{A} & \mathbf{B} \\ \mathbf{B} & \mathbf{D} \end{bmatrix} \begin{bmatrix} \boldsymbol{\varepsilon} \\ \boldsymbol{\kappa} \end{bmatrix} - \Delta T \begin{bmatrix} \mathbf{N}_{\text{th}} \\ \mathbf{M}_{\text{th}} \end{bmatrix}, \tag{3}$$

where $\mathbf{A}$, $\mathbf{B}$ and $\mathbf{D}$ are stiffness matrices. The thermal stress resultants, $\mathbf{N}_{\text{th}}$ and $\mathbf{M}_{\text{th}}$, are obtained as the resultant of the thermal expansion contributions of each of the k layers,

$$\begin{aligned}\mathbf{N}_{\text{th}} &= \sum_k \int_{z_k}^{z_{k+1}} \bar{\boldsymbol{Q}}^{(k)} \boldsymbol{\alpha}^{(k)} \,\mathrm{d}z,\\ \mathbf{M}_{\text{th}} &= \sum_k \int_{z_k}^{z_{k+1}} z\bar{\boldsymbol{Q}}^{(k)} \boldsymbol{\alpha}^{(k)} \,\mathrm{d}z.\end{aligned}$$

The strain energy of the kth layer, per unit surface area, i.e. before integration through the laminate's width and length, is

$$U^{(k)} = \frac{1}{2} \int_{z_k}^{z_{k+1}} \left(\boldsymbol{\epsilon} - \Delta T \boldsymbol{\alpha}^{(k)}\right)^\top \bar{\boldsymbol{Q}}^{(k)} \left(\boldsymbol{\epsilon} - \Delta T \boldsymbol{\alpha}^{(k)}\right) \mathrm{d}z, \tag{4}$$

where z_k and z_{k+1} are the positions of the interfaces between layers. Integrating (4) through thickness and summing over k, we obtain the total strain energy per unit surface area to be

$$U = \frac{1}{2} \begin{bmatrix} \boldsymbol{\varepsilon} \\ \boldsymbol{\kappa} \end{bmatrix}^\top \begin{bmatrix} \mathbf{A} & \mathbf{B} \\ \mathbf{B} & \mathbf{D} \end{bmatrix} \begin{bmatrix} \boldsymbol{\varepsilon} \\ \boldsymbol{\kappa} \end{bmatrix} - \Delta T \begin{bmatrix} \mathbf{N}_{\text{th}} \\ \mathbf{M}_{\text{th}} \end{bmatrix}^\top \begin{bmatrix} \boldsymbol{\varepsilon} \\ \boldsymbol{\kappa} \end{bmatrix} + \frac{U_{\text{th}}}{2} (\Delta T)^2, \tag{5}$$

where

$$U_{\text{th}} = \sum_k \int_{z_k}^{z_{k+1}} \boldsymbol{\alpha}^{(k)\top} \bar{\boldsymbol{Q}}^{(k)} \boldsymbol{\alpha}^{(k)} \,\mathrm{d}z.$$

For convenience, we wish to write the energy in terms of $\boldsymbol{\kappa}$, $\mathbf{N}$ and $\mathbf{N}_{\text{th}}$. To do this, we use the partially-inverted form of (3), which is

$$\begin{bmatrix} \boldsymbol{\varepsilon} \\ \mathbf{M} + \Delta T \mathbf{M}_{\text{th}} \end{bmatrix} = \begin{bmatrix} \mathbf{a} & \mathbf{b} \\ -\mathbf{b}^\top & \mathbf{d} \end{bmatrix} \begin{bmatrix} \mathbf{N} + \Delta T \mathbf{N}_{\text{th}} \\ \boldsymbol{\kappa} \end{bmatrix}, \tag{6}$$

with

$$\mathbf{a} = \mathbf{A}^{-1}, \tag{7a}$$

$$\mathbf{b} = -\mathbf{A}^{-1}\mathbf{B}, \tag{7b}$$

$$\mathbf{d} = \mathbf{D} - \mathbf{B}\mathbf{A}^{-1}\mathbf{B}. \tag{7c}$$

Substituting (6) in (5), we obtain

$$\begin{aligned} U = {} & \frac{1}{2}\boldsymbol{\kappa}^\top \mathbf{d}\boldsymbol{\kappa} - \left(\mathbf{N}_{\text{th}}^\top \mathbf{b} + \mathbf{M}_{\text{th}}^\top\right) \mathbf{d}\boldsymbol{\kappa}\Delta T \\ & + \frac{1}{2}\left((\mathbf{N} - \mathbf{N}_{\text{th}})^\top \mathbf{a}(\mathbf{N} + \mathbf{N}_{\text{th}}) + U_{\text{th}}\right)(\Delta T)^2. \end{aligned}$$

Returning to consider the lattice strips (as opposite to a generic laminate) and assuming, as in Pirrera et al. [6], zero in-plane stress resultants, i.e. $\mathbf{N} = \mathbf{0}$, the strain energy simplifies to

$$U = \frac{1}{2}\boldsymbol{\kappa}^\top \mathbf{d}\boldsymbol{\kappa} - \left(\mathbf{b}^\top \mathbf{N}_{\text{th}} + \mathbf{M}_{\text{th}}\right)^\top \mathbf{d}\boldsymbol{\kappa}\Delta T + \frac{1}{2}\left(U_{\text{th}} - \mathbf{N}_{\text{th}}^\top \mathbf{a}\mathbf{N}_{\text{th}}\right)(\Delta T)^2.$$

Further, it is convenient to define the strip's thermal response parameters,

$$\boldsymbol{\chi} = \mathbf{b}^\top \mathbf{N}_{\text{th}} + \mathbf{M}_{\text{th}}, \tag{8a}$$

$$\tau = U_{\text{th}} - \mathbf{N}_{\text{th}}^\top \mathbf{a} \mathbf{N}_{\text{th}}, \tag{8b}$$

which leads to

$$U = \frac{1}{2}\boldsymbol{\kappa}^\top \mathbf{d}\boldsymbol{\kappa} - \boldsymbol{\chi}^\top \mathbf{d}\boldsymbol{\kappa}\Delta T + \frac{\tau}{2}(\Delta T)^2. \tag{9}$$

3.2. Energy of a unit cell

We now present the energy formulation in terms of the lattice's representative unit cell. Denoting right- and left-handed strips by subscripts + and −, and with reference to Figure 2, the strain energy of the representative unit cell, Π, follows from (9), whence,

$$\begin{aligned}\frac{N}{2\pi}\Pi =& \frac{l}{2}\left(w_+\boldsymbol{\kappa}_+^\top \mathbf{d}_+\boldsymbol{\kappa}_+ + w_-\boldsymbol{\kappa}_-^\top \mathbf{d}_-\boldsymbol{\kappa}_-\right) \\ & - l\left(w_+\boldsymbol{\chi}_+^\top \mathbf{d}_+\boldsymbol{\kappa}_+ + w_-\boldsymbol{\chi}_-^\top \mathbf{d}_-\boldsymbol{\kappa}_-\right)\Delta T + \frac{l}{2}\left(w_+\tau_+ + w_-\tau_-\right)(\Delta T)^2,\end{aligned} \tag{10}$$

where l is the side length of the unit cell and $w_\pm$ the strips' widths.

Following the assumption of Pirrera et al. [6], we consider only axial (x direction) and twist components of curvature. In other words, we neglect the contribution of κ_y to the energy. Intuitively, this seems reasonable for a sufficiently narrow strip. However, a rigorous justification is non-trivial; we refer the reader to [23–26] for a consideration of the issues that arise therein. The analytical simplicity that results from this assumption permits an exploration of the design space and enables a sufficiently accurate understanding of the response characteristics, as evidenced by our experimental and computational demonstration presented in Section 5.4 below.

In addition, the axial and twist components of curvature can be written to account for the strips' reference mechanical stress-free curvature, e.g. a manufacturing or tooling curvature, $\boldsymbol{\upsilon}_\pm$, as

$$\boldsymbol{\kappa}_\pm = \begin{bmatrix}\kappa_{x\pm}(h) \\ \kappa_{xy\pm}(h)\end{bmatrix} - \begin{bmatrix}\upsilon_{x\pm} \\ \upsilon_{xy\pm}\end{bmatrix}, \tag{11}$$

where, from (1),

$$\begin{bmatrix}\kappa_{x\pm}(h) \\ \kappa_{xy\pm}(h)\end{bmatrix} = \frac{1}{R}\begin{bmatrix}\cos^2\theta \\ \pm\sin\theta\cos\theta\end{bmatrix} = \frac{1}{2l^2}\begin{bmatrix}\sqrt{l^2-h^2} \\ \pm h\end{bmatrix}. \tag{12}$$

The bending stiffness, accounting only for axial and twist components of curvature, reduces to

$$\mathbf{d}_\pm = \begin{bmatrix}d_{11\pm} & d_{16\pm} \\ d_{16\pm} & d_{66\pm}\end{bmatrix}.$$

Similarly, $\boldsymbol{\chi}$ reduces to

$$\boldsymbol{\chi} = \begin{bmatrix} \chi_x \\ \chi_{xy} \end{bmatrix}.$$

In the following section, we proceed to express the unit-cell energy in terms of non-dimensional parameters.

4. Normalised energy landscape

We now begin our analysis of the helical lattice, which we will henceforth view as an one-dimensional object whose state is specified by its non-dimensional length and non-dimensional temperature,

$$\bar{h} = \frac{h}{l} \in [0, 1], \tag{13a}$$

$$\overline{T} = \frac{\Delta T}{T_{\text{ref}}}, \tag{13b}$$

respectively. We remark that l might depend on temperature through the in-plane thermal expansion effects captured by τ, however such temperature-induced changes in length are subsumed into $\bar{h}$.

4.1. The energy density

From (10) and (13), the non-dimensionalised energy density, i.e. energy per unit cell, is

$$\begin{aligned} \bar{\Pi} = \frac{4}{\pi} \frac{Nl}{w_+ d_{11+}} \Pi = a_{00} + a_{01}\overline{T} + a_{02}\overline{T}^2 + a_{10}\bar{h} + a_{11}\bar{h}\overline{T} + a_{20}\bar{h}^2 \\ + \sqrt{1 - \bar{h}^2}\left(b_{10} + b_{11}\overline{T} + b_{20}\bar{h}\right), \end{aligned} \tag{14}$$

with coefficients described by

$$\begin{aligned} a_{00} &= 1 + \bar{v}_{x+}^2 + 2\epsilon_+ \bar{v}_{x+}\bar{v}_{xy+} + \delta_+ \bar{v}_{xy+}^2 \\ &\quad + \varphi\left(1 + \bar{v}_{x-}^2 + 2\epsilon_- \bar{v}_{x-}\bar{v}_{xy-} + \delta_- \bar{v}_{xy-}^2\right), \end{aligned} \tag{15a}$$

$$\begin{aligned} a_{01} &= 2T_{\text{ref}} ((\bar{\chi}_{x+}\bar{v}_{x+} + \epsilon_+(\bar{\chi}_{x+}\bar{v}_{xy+} + \bar{\chi}_{xy+}\bar{v}_{x+}) + \delta_+\bar{\chi}_{xy+}\bar{v}_{xy+}) \\ &\quad + \varphi(\bar{\chi}_{x-}\bar{v}_{x-} + \epsilon_-(\bar{\chi}_{x-}\bar{v}_{xy-} + \bar{\chi}_{xy-}\bar{v}_{x-}) + \delta_-\bar{\chi}_{xy-}\bar{v}_{xy-})), \end{aligned} \tag{15b}$$

$$a_{02} = 4\frac{l^2 T_{\text{ref}}^2 \tau_+}{d_{11+}}\left(1 + \frac{w_-\tau_-}{w_+\tau_+}\right), \tag{15c}$$

$$a_{10} = 2\left(\varphi\left(\epsilon_-\bar{v}_{x-} + \delta_-\bar{v}_{xy-}\right) - \left(\epsilon_+\bar{v}_{x+} + \delta_+\bar{v}_{xy+}\right)\right), \tag{15d}$$

$$a_{11} = 2T_{\text{ref}}\left(\varphi\left(\epsilon_-\bar{\chi}_{x-} + \delta_-\bar{\chi}_{xy-}\right) - \left(\epsilon_+\bar{\chi}_{x+} - \delta_+\bar{\chi}_{xy+}\right)\right), \tag{15e}$$

$$a_{20} = \left(\delta_+ - 1\right) + \varphi\left(\delta_- - 1\right), \tag{15f}$$

$$b_{10} = -2\left(\left(\bar{v}_{x+} + \epsilon_+\bar{v}_{xy+}\right) + \varphi\left(\bar{v}_{x-} + \epsilon_-\bar{v}_{xy-}\right)\right), \tag{15g}$$

$$b_{11} = -2T_{\text{ref}}\left(\left(\bar{\chi}_{x+} + \epsilon_+\bar{\chi}_{xy+}\right) + \varphi\left(\bar{\chi}_{x-} + \epsilon_-\bar{\chi}_{xy-}\right)\right), \tag{15h}$$

$$b_{20} = 2\left(\epsilon_+ - \varphi\epsilon_-\right), \tag{15i}$$

utilising the following normalisations,

$$\bar{\boldsymbol{\chi}}_{\pm} = 2l\boldsymbol{\chi}_{\pm}, \tag{16a}$$

$$\bar{\boldsymbol{\kappa}}_{\pm} = 2l\boldsymbol{\kappa}_{\pm}, \tag{16b}$$

$$\bar{\boldsymbol{\upsilon}}_{\pm} = 2l\boldsymbol{\upsilon}_{\pm}, \tag{16c}$$

$$\bar{\varphi} = \frac{w_{-}d_{11-}}{w_{+}d_{11+}} > 0, \tag{16d}$$

$$\bar{\mathbf{d}}_{\pm} = \frac{\mathbf{d}}{d_{11\pm}} = \begin{bmatrix} 1 & \bar{\epsilon}_{\pm} \\ \bar{\epsilon}_{\pm} & \bar{\delta}_{\pm} \end{bmatrix}. \tag{16e}$$

For the stiffness matrix in (16e) to be positive definite, we need $\bar{\delta}_{\pm} > 0$ and $-\sqrt{\bar{\delta}_{\pm}} < \bar{\epsilon}_{\pm} < \sqrt{\bar{\delta}_{\pm}}$. From the energy density (14) we observe that a_{02} is the only term dependent on the in-plane thermal expansion parameter, $\tau_{\pm}$. As such it does not affect the extensional equilibria since it is uncoupled to the extension $\bar{h}$. As a consequence it also does not affect the coefficient of thermal expansion of the structure, see (21) below. The value of a_{02} can therefore be specified arbitrarily. In the examples presented we set $a_{02} = 1$ for convenience.

4.2. Equilibria of the energy density

To identify system equilibria we compute the derivative of the energy density with respect to extension. From (14),

$$\frac{\partial \bar{\Pi}}{\partial \bar{h}} = a_{10} + a_{11}\overline{T} + 2a_{20}\bar{h} + \frac{1}{\sqrt{1-\bar{h}^2}}\left(b_{20} - b_{10}\bar{h} - b_{11}\bar{h}\overline{T} - 2b_{20}\bar{h}^2\right). \tag{17}$$

Inner equilibria. The location of *inner* equilibria, i.e. equilibria for $\bar{h} \in (0,1)$, may be obtained by setting $\frac{\partial \bar{\Pi}}{\partial \bar{h}} = 0$. Temperature-invariant equilibria are obtained when $a_{11} = b_{11} = 0$. Otherwise, the equilibria generically form a quartic curve in $(\bar{h}, \overline{T}) \in (0,1) \times (0,\infty)$. We denote equilibria at temperature $\overline{T}$ (if any) by $\bar{h}_0(\overline{T})$.

Boundary equilibria. The fully-coiled state, $\bar{h} = 0$, is an equilibrium if

$$\left.\frac{\partial \bar{\Pi}}{\partial \bar{h}}\right|_{\bar{h}=0} = b_{20} + a_{10} + a_{11}\overline{T}, \tag{18a}$$

is non-negative. Likewise, the fully-extended state, $\bar{h} = 1$, is an equilibrium if

$$\begin{cases} \operatorname{sgn} \left.\frac{\partial \bar{\Pi}}{\partial \bar{h}}\right|_{\bar{h}\to 1} = -\operatorname{sgn}(b_{10} + b_{20} + b_{11}\overline{T}) & \text{if} \quad b_{10} + b_{20} + b_{11}\overline{T} \neq 0, \\ \operatorname{sgn} \left.\frac{\partial \bar{\Pi}}{\partial \bar{h}}\right|_{\bar{h}=1} = \operatorname{sgn}(a_{10} + 2a_{20} + a_{11}\overline{T}) & \text{if} \quad b_{10} + b_{20} + b_{11}\overline{T} = 0, \end{cases} \tag{18b}$$

is non-positive.

As above, temperature-invariant equilibria are obtained when $a_{11} = b_{11} = 0$. On the other hand, when $a_{11} \neq 0$ and $b_{11} \neq 0$, from the linear dependence on $\overline{T}$ in (18a) and (18b), we conclude that an equilibrium appears or disappears at each boundary precisely once if temperature is varied monotonically. This occurs at the temperatures

$$\overline{T}_0 = -\frac{a_{10} + b_{20}}{a_{11}}, \tag{19a}$$

$$\overline{T}_1 = -\frac{b_{10} + b_{20}}{b_{11}}, \tag{19b}$$

for $\bar{h} = 0$ and $\bar{h} = 1$, respectively. Whether an equilibrium appears or disappears depends on sign of a_{11} and b_{11} (and, of course, the direction of the temperature change). Note also that $\bar{h} = 0$ is an equilibrium at $\overline{T} = \overline{T}_0$, but whether $\bar{h} = 1$ is an equilibrium at $\overline{T} = \overline{T}_1$ depends on the sign of $a_{10} + 2a_{20} + a_{11}\overline{T}_1$ (cf., (18b) and (19b)).

4.3. Extensional stiffness

The effective stiffness of the system is the second derivative of the energy with respect to extension. From (17),

$$\frac{\partial^2 \overline{\Pi}}{\partial \bar{h}^2} = 2a_{20} + \frac{1}{\left(1 - \bar{h}^2\right)^{3/2}} \left(-b_{10} - b_{11}\overline{T} - 3b_{20}\bar{h} + 2b_{20}\bar{h}^3\right). \tag{20}$$

We remark that it is possible, using (17) and (20), to tune the lattice to possess a zero stiffness state at a specified temperature. This feature can be useful for actuation by means of input parameters other than temperature, as it minimises the energy required for shape changes induced, for example, by mechanical or piezoelectric stimuli.

Stability of equilibria.. The stability of inner equilibria can be deduced from the sign of (20), provided it is non-zero.

From the discussion on boundary equilibria in Section 4.2, it follows that the boundary equilibria are stable (when they exist) except possibly at the critical temperatures $\overline{T} = \overline{T}_0$ and $\overline{T} = \overline{T}_1$, for $\bar{h} = 0$ and $\bar{h} = 1$, respectively. Thus, during a temperature sweep, once a critical temperature is passed and an equilibrium has appeared at a boundary, it will remain stable until the direction of the temperature sweep is reversed and the critical temperature is passed again. This behaviour is beneficial from a thermal actuation standpoint, because it ensures that the system remains in one state once actuation has occurred.

4.4. Coefficient of Thermal Expansion

The non-dimensional coefficient of thermal expansion (CTE) for the system may be defined as

$$\frac{\partial \bar{h}_0}{\partial \overline{T}}, \tag{21}$$

where $\bar{h}_0 \in (0,1)$ is a solution of (17). An explicit expression for the CTE can be obtained from (17) but, for brevity, we prefer to present numerical examples in Section 5 below.

In order to avoid apparently infinite thermal expansions when $\bar{h}_0$ approaches zero, (21) omits the reciprocal of initial length $\frac{1}{\bar{h}_0}$ and, instead, a nominal value of one is used corresponding to the total non-dimensional length of the lattice strip. (However, when discussing experimental results the usual definition of CTE is applied.) Equation (21) is non-zero only when either $a_{11} \neq 0$ or $b_{11} \neq 0$. Moreover the CTE can be zero at $\bar{h}_0 = 0$ and $\bar{h}_0 = 1$ due to the stability conditions of the boundary (cf. last paragraph of Section 4.2).

We remark that the CTE referred to here neglects changes in length of the structure due to the effect of temperature on l, which effect is characterised by τ defined in (8b). In general, the physical length $\bar{h}_0$ of the structure will change with temperature even for zero non-dimensional CTE. However, these changes will be small in comparison to the overall deformation and can be neglected. In other words, when the magnitude of CTE is large, as in Figures 5, 6 and 7, the change in length due to in plane expansion would typically be dwarfed by the large CTE. Moreover, the possibility remains that the structure could be designed such that its non-dimensional CTE cancels the change in length due to the constituent materials' thermal expansion. Such a structure would be completely thermally invariant.

5. Thermoelastic Behaviour

The thermoelastic response of the lattice may be tailored to fall into two categories, snapping actuation and smooth actuation. In the first instance, the lattice undergoes a large extension/contraction upon heating/cooling to critical temperatures. Such sudden transitions occur when an equilibrium looses stability, forcing the system to reconfigure by snapping onto a new stable state across the energy landscape. Alternatively, extension and contraction can be smooth transitions. In these instances, stable equilibria change position gradually, maintaining their stability as the temperature varies.

Either kind of response may be desirable. Snapping actuation, for example, can replicate the typical behaviour of SMAs. However, as we shall see below, the lattice's critical temperatures, direction of actuation, effective stiffness and presence of hysteresis between cooling and heating actuation points, can all be simultaneously tuned far beyond that of SMAs.

Table 1 presents the coefficients utilised in the examples in this section. These values are illustrative, rather than restrictive, and are selected to demonstrate system responses that appear robustly in parameter space while facilitating analysis by simplifying (15). In addition, the choice of parameters ensures realistic material properties and feasible structural designs.

Our analysis is in terms of the 'a' and 'b' coefficients defined in (15). Since the non-dimensionalised energy density (14) can be written as a simple function of these coefficients, this facilitates the following analysis of the conditions under which we obtain snap actuation, smooth actuation and phase transitions. However, it

			All curvature parameters scaled by $\times 10^4$							
Fig.	$\overline{T}_0$	$\overline{T}_1$	$\bar{\chi}_x^+$	$\bar{\chi}_x^-$	$\bar{\nu}_x^+$	$\bar{\nu}_x^-$	$\bar{\chi}_{xy}^+$	$\bar{\chi}_{xy}^-$	$\bar{\nu}_{xy}^+$	$\bar{\nu}_{xy}^-$
3b	-0.2	-0.3	-1	-1	$\bar{T}_1 T_{\text{ref}}$	$\bar{T}_1 T_{\text{ref}}$	2	1	$-2\bar{T}_0 T_{\text{ref}}$	$-\bar{T}_0 T_{\text{ref}}$
4a	-0.2	-0.2	-1	-1	$\bar{T}_1 T_{\text{ref}}$	$\bar{T}_1 T_{\text{ref}}$	2	1	$-2\bar{T}_0 T_{\text{ref}}$	$-\bar{T}_0 T_{\text{ref}}$
4b	-0.2	-0.2	1	1	$-\bar{T}_1 T_{\text{ref}}$	$-\bar{T}_1 T_{\text{ref}}$	-2	-1	$2\bar{T}_0 T_{\text{ref}}$	$\bar{T}_0 T_{\text{ref}}$
5 (red)	-0.35	0	-1	-1	$\bar{T}_1 T_{\text{ref}}$	$\bar{T}_1 T_{\text{ref}}$	2	1	$-2\bar{T}_0 T_{\text{ref}}$	$-\bar{T}_0 T_{\text{ref}}$
5 (blue)	0.0	-0.35	1	1	$-\bar{T}_1 T_{\text{ref}}$	$-\bar{T}_1 T_{\text{ref}}$	-2	-1	$2\bar{T}_0 T_{\text{ref}}$	$\bar{T}_0 T_{\text{ref}}$
5 (black)	-0.1	-0.1	-1	-1	$\bar{T}_0 T_{\text{ref}}$	$\bar{T}_0 T_{\text{ref}}$	-4	-2	$4\bar{T}_0 T_{\text{ref}}$	$2\bar{T}_0 T_{\text{ref}}$

Table 1: Non-dimensional system parameters with critical temperatures $\overline{T}_0$ and $\overline{T}_1$ for the examples presented. In all cases $\delta_\pm = 1$, $\epsilon_\pm = 0$, $a_{20} = 1$, $\bar{\varphi} = 1$ and $T_{\text{ref}} = 453\,\text{K}$.

would be more useful to a designer if the resulting criteria for these qualitatively-different behaviours could be expressed in terms of the geometric and material parameters in (16). Unfortunately, since the map (15) from geometric/material parameters to a/b parameters is nonlinear a non-numerical analysis in terms of the geometric/material parameters is not feasible. In practise, a designer would have to combine the analysis below with a numerical investigation of the consequent restrictions on the geometric/material parameters.

5.1. Snap Actuation.

The stability of the system at the extremes of extension, i.e., when it is either fully coiled or fully extended, can be exploited to produce snapping actuation. Figure 3 illustrates snap-actuation from fully-coiled to fully-extended states upon heating to a critical temperature, $\overline{T}_0$. Snap-back to the fully-coiled state happens upon cooling to a critical temperature, $\overline{T}_1$, which is no higher than $\overline{T}_0$. Such an actuator mimics an SMA's behaviour. The temperatures $\overline{T}_0$ and $\overline{T}_1$ are related to the coefficients in (14) through (19a) and (19b). The conditions on the coefficients under which snapping behaviour is guaranteed are:

- The fully-coiled configuration, $\bar{h} = 0$, is stable if and only if $\overline{T} < \overline{T}_0$, and the fully-extended configuration, $\bar{h} = 1$, is stable if and only if $\overline{T} > \overline{T}_1$. From (18) and (19), this implies,

  $$a_{11} < 0, \tag{22a}$$

  $$b_{11} > 0, \tag{22b}$$

  respectively.

- The temperature above which the fully-coiled configuration loses stability, $\overline{T}_0$, is greater than the temperature above which the fully-extended state gains stability, $\overline{T}_1$:

  $$\overline{T}_0 > \overline{T}_1. \tag{23}$$

- In addition, for the equilibrium to shift from $\bar{h} = 0$ to $\bar{h} = 1$ as the temperature is increased to $\overline{T}_0$, we require

  $$\frac{\partial \bar{\Pi}(T_0, h)}{\partial \bar{h}} < 0 \quad \forall\, \bar{h} \in (0, 1),$$

  which, from (17) and (19a), can be cast as

  $$-b_{20} + 2a_{20}\bar{h} + \frac{1}{\sqrt{1-\bar{h}^2}}\left(b_{20} - b_{10}\bar{h} + b_{11}\left(\frac{a_{10} + b_{20}}{a_{11}}\right)\bar{h} - 2b_{20}\bar{h}^2\right) < 0, \quad \forall\, \bar{h} \in (0, 1). \tag{24a}$$

- Similarly, for the equilibrium to shift from $\bar{h} = 1$ to $\bar{h} = 0$ as the temperature is decreased to $\overline{T}_1$, we require

  $$\frac{\partial \bar{\Pi}(T_1, h)}{\partial \bar{h}} > 0 \quad \forall\, \bar{h} \in (0, 1),$$

  or equivalently, using (17) and (19b), that

  $$a_{10} - a_{11}\left(\frac{b_{20} + b_{10}}{b_{11}}\right) + 2a_{20}\bar{h} + \frac{b_{20}}{\sqrt{1-\bar{h}^2}}\left(1 + \bar{h} - 2\bar{h}^2\right) > 0, \quad \forall\, \bar{h} \in (0, 1). \tag{24b}$$

In summary, equations (22), (23) and (24) are the conditions under which the system exhibits hysteretic snap actuation.

If, as a special case which simplifies (24) by removing the dependency on $\bar{h}$, we assume that

$$a_{20} = 0, \tag{25a}$$

$$b_{20} = 0, \tag{25b}$$

then (24) is equivalent to

$$-b_{10} + b_{11}\frac{a_{10}}{a_{11}} < 0, \tag{26a}$$

$$a_{10} - a_{11}\frac{b_{10}}{b_{11}} > 0. \tag{26b}$$

In other words, when (25) holds, equations (22), (23) and (24) can be replaced by equations (22), (23) and (26). However, using (19), it is easy to verify that (22) and (23) imply (26). Thus, equations (22), (23) and (24) can be replaced by equations (22), (23) and (25).

For the lattice in Figure 3b, as temperature increases, the fully-coiled state is stable until temperature $\overline{T}_0 = -0.2$, at which point the lattice snaps to the fully-extended state. Upon cooling, the extended state loses stability at $\overline{T}_1 = -0.3$ and the lattice snaps back to the fully-coiled state. Consequently, the structure demonstrates hysteresis, being bi-stable in the range $[\overline{T}_1, \overline{T}_0] = [-0.3, -0.2]$ and monostable elsewhere.

The removal of thermal hysteresis for SMAs requires subtle fine-tuning of the atomic lattice [27–29]. In contrast, the system presented herein can be readily tuned to be hysteresis-free by setting $\overline{T}_0 = \overline{T}_1$, as

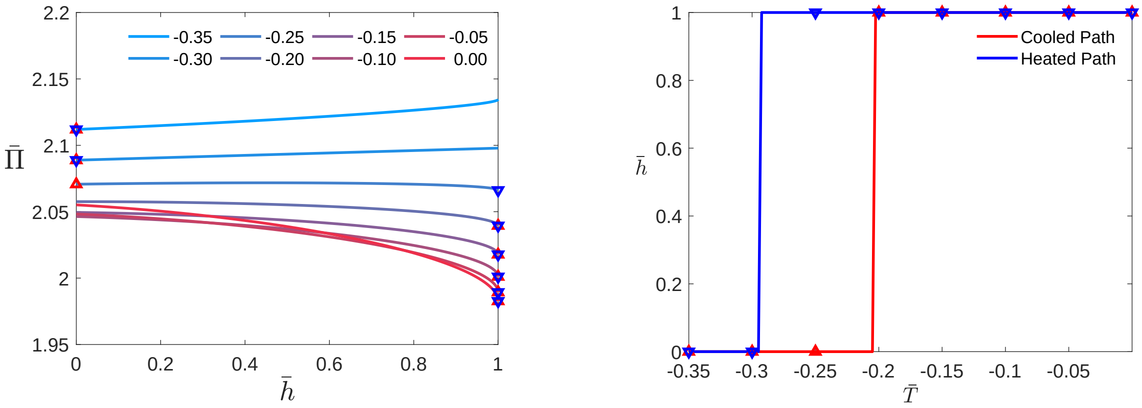

(a) Energy landscape and equilibrium position for temperatures indicated by the label on the curves. Markers correspond to stable equilibria. $\bar{h} = 0$ is stable below $\overline{T} = -0.2$ and $\bar{h} = 1$ is stable above $\overline{T} = -0.3$. Red and blue markers indicate lattice length upon heating and cooling, respectively.

(b) Equilibrium paths for heating and cooling for the energy landscape in (a).

Figure 3: (a) Energy landscapes for various $\overline{T}$ and (b) corresponding temperature-extension profile.

illustrated in Figures 4a and 4b. Generically, the conditions

$$\overline{T}_0 = -\frac{a_{10}}{a_{11}} = -\frac{b_{10}}{b_{11}} = \overline{T}_1,$$

$$a_{20} = 0 = b_{20},$$

$$a_{11} < 0 < b_{11}.$$

suffice to guarantee hysteresis-free shape memory behaviour. Moreover, the direction of actuation may be reversed by choosing $a_{11} > 0 > b_{11}$ (contrast Figures 4a and 4b).

5.2. Smooth Actuation.

The preceding examples achieve snap-actuation at a critical temperature through appearance or disappearance of equilibria at the extensional boundaries, i.e. when the lattice is either fully coiled or fully extended. Conversely, smooth actuation is obtained by exploiting stable inner equilibria, i.e. at partial extension. This behaviour is illustrated in Figure 5 for positive-CTE (red curve) and negative-CTE (blue curve) lattices. The existence of inner equilibria can be guaranteed by imposing suitable signs on the derivative of the energy on the boundary [6]. The resulting effective CTEs, both positive and negative, illustrated in Figure 5b, can be tailored by tuning the system parameters.

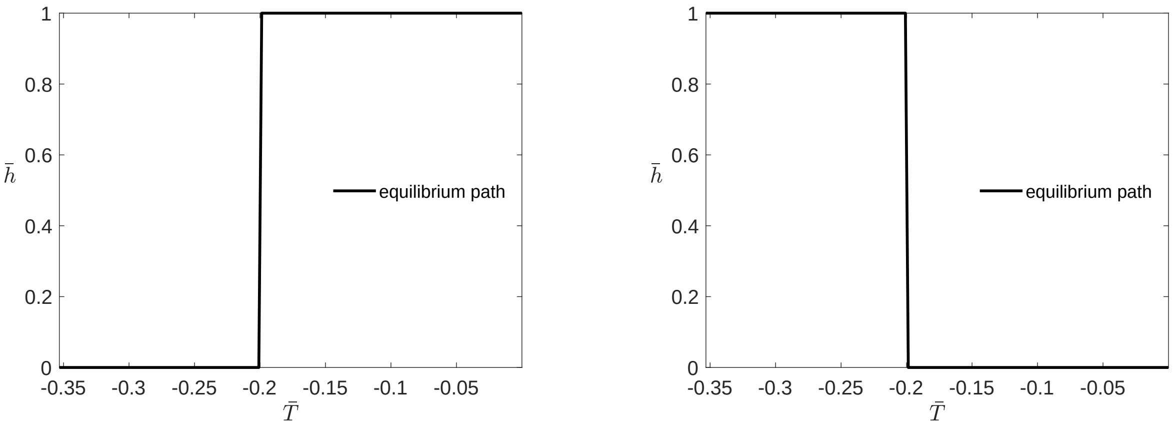

(a) Snap open actuation with no hysteresis from coiled to extended for increasing $\overline{T}$.

(b) Snap closed actuation with no hysteresis from extended to coiled for increasing $\overline{T}$.

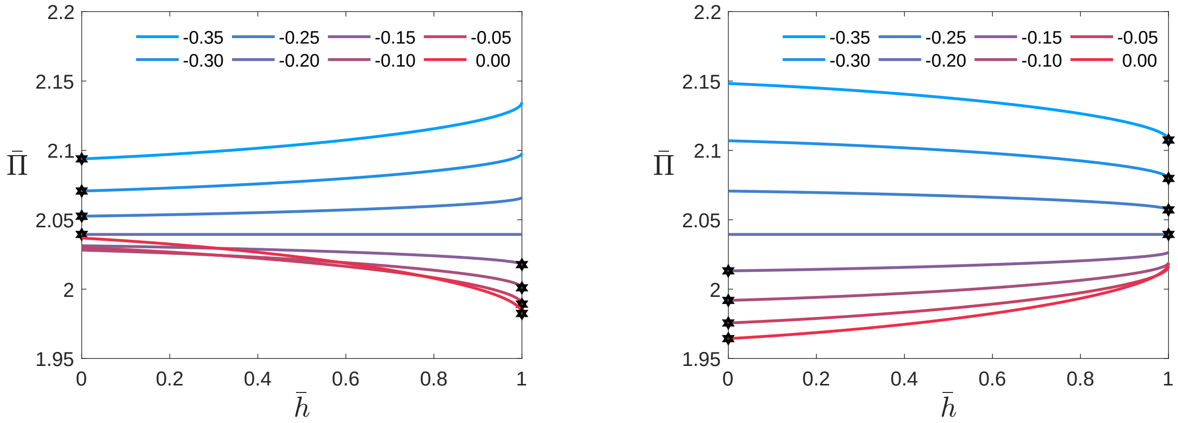

(c) Energy landscape with hysteresis-free snap open a flat energy landscape is observed at $T = -0.2$.

(d) Energy landscape with hysteresis-free snap closed a flat energy landscape is observed at $T = -0.2$.

Figure 4: (a) and (b) Temperature-extension profiles for two other lattices illustrating hysteresis-free shape memory behaviour. $\overline{T}$ is the fractional change from a reference temperature and $\bar{h}$ the fractional cell extension. (c) and (d) illustrate the energy profiles for the forward and backwards actuation. Temperatures are indicated by the label on the curves. Markers correspond to stable equilibria.

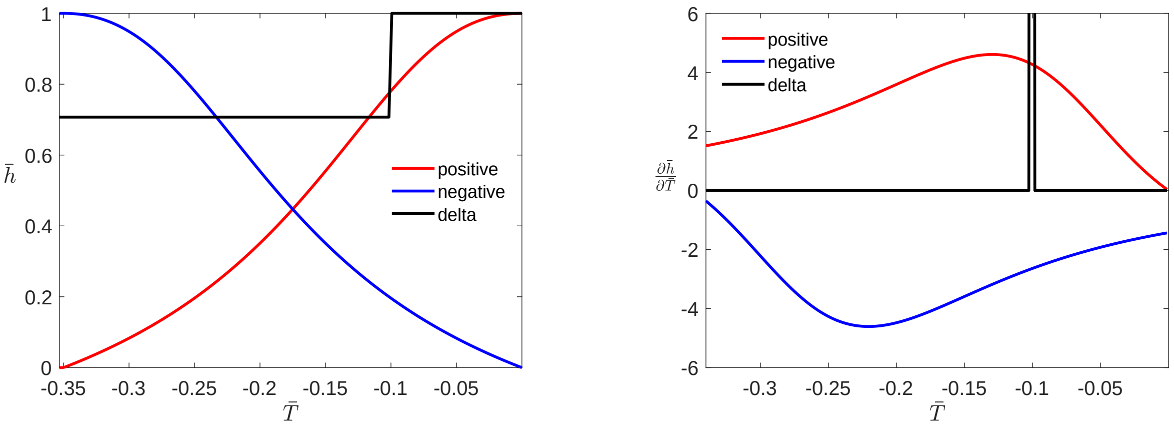

(a) Lattice length for changing temperature.

(b) Non-dimensional CTEs.

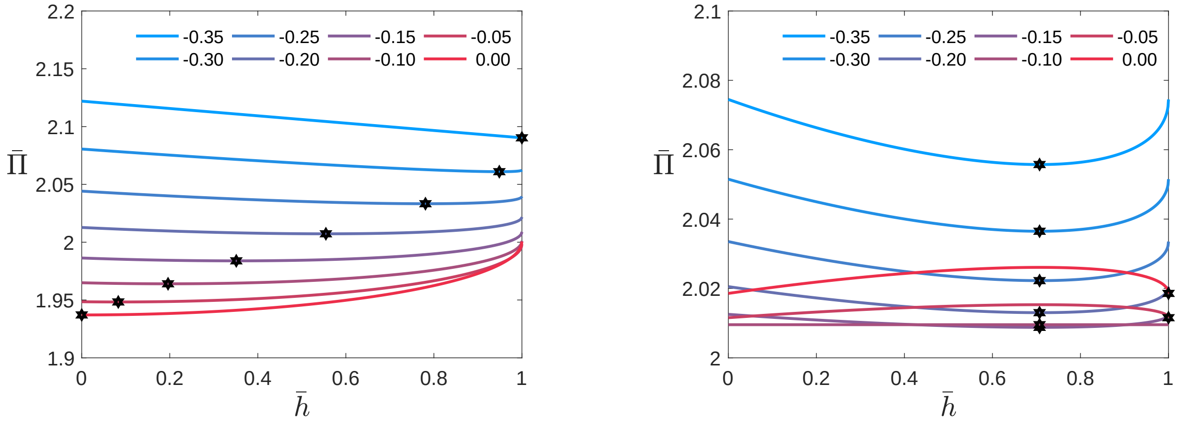

(c) Energy landscape and smooth transition of single equilibrium position for negative CTE.

(d) Energy landscape and equilibrium position for Dirac-Delta CTE. Single equilibria observed when $\overline{T} < -0.1$ and bi-stable for $\overline{T} > -0.1$.

Figure 5: (a) Temperature-extension profiles and (b) non-dimensional CTEs and for three different lattices demonstrating positive (red), negative (blue) and Dirac-delta (black) CTEs. $\overline{T}$ is the fractional change from a reference temperature and $\bar{h}$ the fractional extension, i.e. $\bar{h} = 0$ is a fully coiled lattice and $\bar{h} = 1$ fully extended. (c) and (d) illustrate the energy profiles for the negative and Dirac-delta CTEs. Temperatures are indicated by the label on the curves. Markers correspond to stable equilibria. (d) Above the critical temperature $\overline{T} = -0.1$ the Dirac-Delta's choice of equilibrium state is dictated by numerical accuracy - both fully coiled and extended are feasible.

5.3. Phase transitions.

In addition to tailoring the magnitude and direction of effective CTE, we can devise a system which is mono-stable (with an interior equilibrium) but develops bi-stability at a critical temperature—in other words, mimics the austenite-martensite transformation that a one-dimensional SMA would exhibit. To this end, consider the choice of parameters

$$\begin{aligned} a_{20} &= b_{20} = 0, \\ a_{11} &= r b_{11} \neq 0, \\ a_{10} &= r b_{10}, \end{aligned}$$

for some non-zero r. The resulting system has a stable equilibrium at fractional extension $\bar{h} = \frac{1}{\sqrt{1+r^2}}$ for $\overline{T} < -\frac{a_{10}}{a_{11}}$. At $\overline{T} = -\frac{a_{10}}{a_{11}}$ the energy becomes independent of $\bar{h}$, i.e. every fractional extension is stable. If the temperature is increased further, the equilibrium at $\bar{h} = \frac{1}{\sqrt{1+r^2}}$ becomes unstable and stable equilibria appear at the boundaries, i.e. $\bar{h} = 0$ and $\bar{h} = 1$. These boundary equilibria remain stable as the temperature is increased further. Note that, unlike in SMAs, the mono-stable state need not be the high-temperature state.

As a consequence, the CTE is zero except at the critical temperature of $\overline{T} = -\frac{a_{10}}{a_{11}}$ (see the black curve in Figure 5b, where $r = 1$). At this critical temperature, the system's length instantaneously changes from $\bar{h}_0 = \frac{1}{\sqrt{2}}$ to either 0 or 1. Thus the CTE is a Dirac-delta with a multiplicative pre-factor of either $-\frac{1}{\sqrt{2}}$ or $(1 - \frac{1}{\sqrt{2}})$.

Moreover, the flat energy landscape at the critical temperature, with the consequent zero-stiffness, results in minimal actuation energy to move from one extension to another. This feature is desirable (quite apart from considerations of thermal expansion) in morphing applications since the system could be actuated in its zero-stiffness state, requiring minimal energy input, and then allowed to return to its normal state, with a corresponding increase in stiffness.

5.4. Experimental Demonstration.

We now present an experimental demonstration of the smooth actuation behaviour.

The prototype, illustrated in Figure 1, was tuned to exhibit a large negative CTE. The design, with full details discussed in appendix Appendix A, was selected for ease of manufacturability rather than optimal performance. The thermal behaviour of the lattice was obtained by tracking its expansion from a heated state as it cooled while suspended horizontally in an oven, see Figures 6a and 6b. The temperature of the structure was obtained using a thermal imaging camera and multiple thermocouples, and shown to be uniform. The apparent variation in temperature shown in the heat maps can be explained by varying incidence angles and distances from the prototype to the camera. The total extension of the lattice was extracted from video images tracking the position of the nodes of the unit cells.

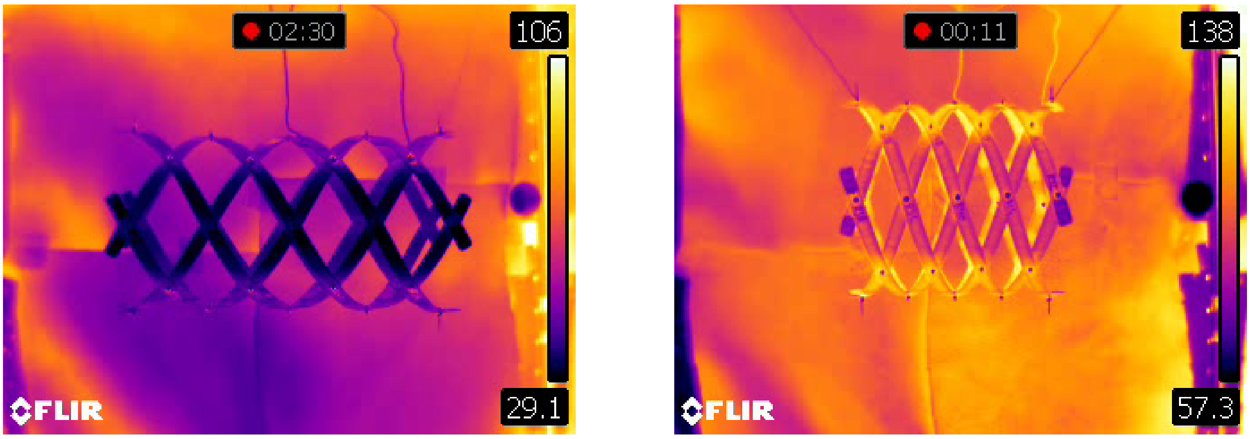

(a) Lattice in relatively extended state at low temperature of about 310 K.

(b) Lattice in relatively contracted state at high temperature of about 410 K.

Figure 6: Heat maps from thermal imaging camera showing the lattice prototype at the start and end of motion. Colour bar in °C.

The width of the lattice's strips is 10 mm, which is larger than desirable in light of the one-dimensional strip behaviour assumed by the analytical model, but simplifies manufacturing. For this reason, we also include results obtained using an ABAQUS finite element (FE) simulation (quasi-static, geometrically nonlinear analysis with `S4R` shell elements), which will represent the experiment more closely. Figure 7 shows clear correlation between the FE, analytical and experimental results. As expected, the correlation between the analytical prediction and the FE simulation improves as the width of the strip is reduced from 10 mm to 0.5 mm to better approximate one-dimensional behaviour. The residual difference between the analytical prediction and the latter FE simulation can be attributed to other approximations in the analytical model.

6. Conclusions

The analyses and prototype presented herein demonstrate how a structure, in this case, a helical lattice, can be designed to mimic a one-dimensional thermoelastic material.

We have illustrated how the design parameters can be tuned to achieve effective behaviour that mimics that of phase-transforming materials such as SMAs. Indeed, we can more than mimic such materials, improving overall behaviour by, e.g., extending functionality. We can easily tune parameters such as transition temperatures, which are much more difficult to design at the crystalline microstructure scale through materials science. Further, it is no more difficult to reduce and even eliminate hysteresis as required. In contrast, eliminating hysteresis in SMAs requires considerable expertise [27–29]. With the proposed system, even the direction of actuation can be reversed.

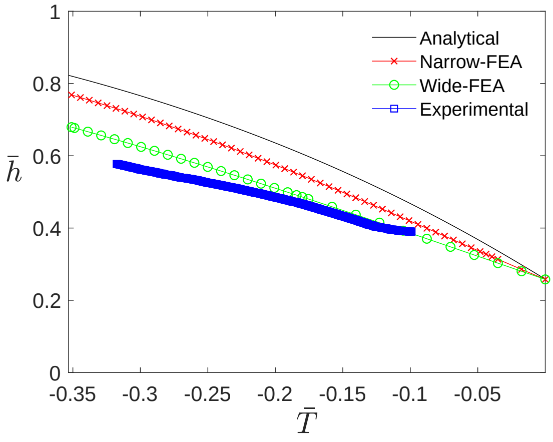

Figure 7: Fractional length of lattice as a functional of fractional temperature as predicted by analysis (black), simulated by FE (red and green) and measured by experiments (blue). The wide-FEA corresponds to a 10 mm strip and the narrow-FEA to a 0.5 mm strip.

Turning to thermoelasticity more broadly, we can design for: zero and negative CTEs; for CTE magnitudes, both positive and negative, beyond what has been observed in nature; and for Dirac-delta CTEs. As a demonstration of the capabilities of this design approach we manufactured a thermoelastic lattice with a large negative CTE.

The examples presented are only a brief foray into the capacity to tune the coefficient of thermal expansion and extensional stiffness. In general, the relationship between CTE and extensional stiffness can be deduced from Equation (14), which can be exploited to overcome the difficulties incurred using traditional approaches in obtaining a system with desirable CTE and stiffness [18].

Finally, we note that, although the present approach focuses specifically on thermal actuation, any curvature-inducing field could be utilised instead; for example, electric fields in conjunction with piezoelectric materials.

In conclusion, we have outlined a structural route to attain and exceed capabilities which are typically associated with multi-phase materials such as SMAs or architectured materials with negative CTEs. In this flipped design paradigm the structure acts as a material.

Data access statement

The data necessary to support the conclusions are included in the paper.

Acknowledgements

This research was supported by the Engineering and Physical Sciences Research Council (EPSRC) through the University of Bristol's Centre for Doctoral Training in Advanced Composites for Innovation and Science [Grant No. EP/L016028/1] and Alberto Pirrera's EPSRC Early Career Research Fellowship [Grant No. EP/M013170/1]. The authors express their gratitude to the reviewers for their detailed comments and questions that have helped to provided additional clarity to the content of the manuscript.

Appendix A. Supplementary Experimental Information

Determination of the physical parameters that give desired non-dimensional coefficients (15) is non-trivial due to the non-linear relationship between ply-angles and reduced stiffness matrix **d** for a composite system. Characterising the feasible domain is necessarily material dependent and a robust design would also need careful consideration of failure criteria and manufacturability restrictions. Addressing these difficulties and developing a robust, optimised design framework remains an ongoing area of investigation.

Lacking an elegant solution, the design of the helical lattice prototype was instead selected using a semi-exhaustive search process to select design parameters of ply-angles characterising the layup and the tool alignment to tailor the pre-stress. A cylindrical tool shape was assumed, this was chosen due to manufacturing difficulties associated with laying-up on non-developable surfaces. The tool radius and cell lengths were selected based on manufacturing experience, and preliminary analysis in ABAQUS. Choice of cell-size and tooling curvature was limited by available equipment and in response to difficulties encountered during hand assembly of the pre-stress strips into the helical configuration. The tool angle reflected the strips alignment on the cylindrical tool-surface and was considered a free design variable (circumferential wrapping being 0). The choice of ply-angles that comprise the layup allowed tailoring of the stiffness and thermal curvatures of the strips. Both ply angles and tool angle were restricted to 5 degree increments to reflect nominal manufacturing accuracy.

Using the properties specified in Table A.2, the lattice's stiffness parameters are

$$\mathbf{d}_{+} = \begin{bmatrix} 0.4360 & -0.1222 \\ -0.1222 & 0.0968 \end{bmatrix} \text{Nm}, \qquad \mathbf{d}_{-} = \begin{bmatrix} 0.4360 & 0.1222 \\ 0.1222 & 0.0968 \end{bmatrix} \text{Nm}.$$

The thermal and mechanical curvature for this system are,

$$\boldsymbol{\chi}_{+} = \begin{bmatrix} 0.0400 \\ -0.0214 \end{bmatrix} \text{m}^{-1}, \qquad \boldsymbol{\chi}_{-} = \begin{bmatrix} 0.0400 \\ 0.0214 \end{bmatrix} \text{m}^{-1},$$

$$\boldsymbol{\upsilon}_{+} = \begin{bmatrix} 12.2386 \\ 3.2793 \end{bmatrix} \text{m}^{-1}, \qquad \boldsymbol{\upsilon}_{-} = \begin{bmatrix} 12.2386 \\ -3.2793 \end{bmatrix} \text{m}^{-1}.$$

E_{11}	161 GPa	E_{22}	11.38 GPa
G_{12}	5.17 GPa	ν_{12}	0.32
α_{11}	-0.1×10^{-6} 1/K	α_{22}	31.0×10^{-6} 1/K
N	4	$w_{\pm}$	10 mm
Layup$_{+}$	[-15, -70, -35, 90]	Layup$_{-}$	[+15, +70, +35, 90]
Ply Thickness	0.1177 mm	Tool Radius	76 mm
Tool Angle	15°	Cell Length	62 mm

Table A.2: Properties of the prototype. The material properties of the strips (IM7-8552) were obtained from literature [30] and in-house measurement. The ply-angles listed left-to-right describe the laminate stacking sequence from the tool surface outwards. A mirror symmetry between the left- and right-handed strips was imposed to reduce the design space.

a_{00}	3.6155	$\bar{\chi}_{x+}$	0.0032	δ_{+}	0.2219
a_{01}	5.7663	$\bar{\chi}_{x-}$	0.0032	δ_{-}	0.2219
a_{02}	18.7260	$\bar{\upsilon}_{x+}$	0.9659	ϵ_{-}	-0.2802
a_{10}	0.8529	$\bar{\upsilon}_{x-}$	0.9659	ϵ_{+}	0.2802
a_{11}	2.2840	$\bar{\chi}_{xy+}$	-0.0017	$\bar{\varphi}_{+}$	1.0000
a_{20}	-1.5562	$\bar{\chi}_{xy+}$	0.0017		
b_{10}	-3.5736	$\bar{\upsilon}_{xy+}$	0.2588		
b_{11}	-6.5817	$\bar{\upsilon}_{xy+}$	-0.2588		
b_{20}	-1.1208				

Table A.3: Non-dimensional coefficients utilised for comparison with the experimental analysis.

The geometric parameter $l = 0.0395$ m is calculated using the cell length, $T_{\text{ref}} = 453$ K is the nominal cure temperature and $\tau_{\pm} = 0.0032$ NmK^{-2}; a_{02} in (15c) can be calculated from these values.

Finally, from the values presented above, we obtain the non-dimensional description of the system presented in Table A.3.

References

[1] K. Bhattacharya, R. D. James, The material is the machine, Science 307 (5706) (2005) 53–54.

[2] O. Sigmund, S. Torquato, Composites with extremal thermal expansion coefficients, Applied Physics Letters 69 (21) (1996) 3203–3205.

[3] W. Miller, C. Smith, D. S. Mackenzie, K. E. Evans, Negative thermal expansion: A review, Journal of Materials Science 44 (2009) 5441–5451.

[4] P. Tao, W. Shang, C. Song, Q. Shen, F. Zhang, Z. Luo, N. Yi, D. Zhang, T. Deng, Bioinspired engineering of thermal materials, Advanced Materials 27 (3) (2015) 428–463.

[5] E. Boatti, N. Vasios, K. Bertoldi, Origami metamaterials for tunable thermal expansion, Advanced Materials 29 (26) (2017) 1700360.

[6] A. Pirrera, X. Lachenal, S. Daynes, P. M. Weaver, I. V. Chenchiah, Multi-stable cylindrical lattices, Journal of Mechanics Physics of Solids 61 (2013) 2087–2107.

[7] G. D. Barrera, J. A. O. Bruno, T. H. K. Barron, N. L. Allan, Negative thermal expansion, Journal of Physics: Condensed Matter 17 (4) (2005) R217.

[8] A. Pirrera, D. Avitabile, P. M. Weaver, Bistable plates for morphing structures: A refined analytical approach with high-order polynomials, International Journal of Solids and Structures 47 (25-26) (2010) 3412–3425.

[9] Z. Chen, Q. Guo, C. Majidi, W. Chen, D. J. Srolovitz, M. P. Haataja, Nonlinear geometric effects in mechanical bistable morphing structures, Physical Review Letters 109 (11) (2012) 114302.

[10] P. Wang, J. Shim, K. Bertoldi, Effects of geometric and material nonlinearities on tunable band gaps and low-frequency directionality of phononic crystals, Physical Review B 88 (1) (2013) 014304.

[11] F. Fraternali, G. Carpentieri, A. Amendola, On the mechanical modeling of the extreme softening/stiffening response of axially loaded tensegrity prisms, Journal of the Mechanics and Physics of Solids 74 (Supplement C) (2015) 136–157.

[12] M. P. O'Donnell, P. M. Weaver, A. Pirrera, Can tailored non-linearity of hierarchical structures inform future material development?, Extreme Mechanics Letters 7 (2016) 1–9.

[13] K. Bertoldi, Harnessing instabilities to design tunable architected cellular materials, Annual Review of Materials Research 47 (1) (2017) 51–61.

[14] L. Xia, P. Breitkopf, Recent advances on topology optimization of multiscale nonlinear structures, Archives of Computational Methods in Engineering 24 (2) (2017) 227–249.

[15] R. Groh, D. Avitabile, A. Pirrera, Generalised path-following for well-behaved nonlinear structures, Computer Methods in Applied Mechanics and Engineering 331 (2018) 394–426.

[16] F. Dewalque, C. Schwartz, V. Denoël, J.-L. Croisier, B. Forthomme, O. Brüls, Experimental and numerical investigation of the nonlinear dynamics of compliant mechanisms for deployable structures, Mechanical Systems and Signal Processing 101 (Supplement C) (2018) 1–25.

[17] M. Z. Miskin, K. J. Dorsey, B. Bircan, Y. Han, D. A. Muller, P. L. McEuen, I. Cohen, Graphene-based bimorphs for micron-sized, autonomous origami machines, Proceedings of the National Academy of Sciences 115 (3) (2018) 466–470.

[18] G. Jefferson, T. A. Parthasarathy, R. J. Kerans, Tailorable thermal expansion hybrid structures, International Journal of Solids and Structures 46 (11) (2009) 2372–2387.

[19] K. Takenaka, Negative thermal expansion materials: technological key for control of thermal expansion, Science and Technology of Advanced Materials 13 (1) (2012) 013001.

[20] D. Das, T. Jacobs, L. J. Barbour, Exceptionally large positive and negative anisotropic thermal expansion of an organic crystalline material, Nature Materials 9 (2010) 36–39.

[21] A. D. Fortes, E. Suard, K. S. Knight, Negative linear compressibility and massive anisotropic thermal expansion in methanol monohydrate, Science 331 (6018) (2011) 742–746.

[22] E. H. Mansfield, The bending and stretching of plates, 2nd Edition, Cambridge University Press, Cambridge, UK, 2005.

[23] M. A. Dias, B. Audoly, "Wunderlich, meet Kirchhoff": A general and unified description of elastic ribbons and thin rods, Journal of Elasticity 119 (1) (2015) 49–66.

[24] L. Freddi, P. Hornung, M. G. Mora, R. Paroni, A corrected Sadowsky functional for inextensible elastic ribbons, Journal of Elasticity 123 (2) (2016) 125–136.

[25] L. Freddi, P. Hornung, M. Giovanna Mora, R. Paroni, A variational model for anisotropic and naturally twisted ribbons,

SIAM Journal on Mathematical Analysis 48 (6) (2016) 3883–3906.

[26] R. Paroni, G. Tomassetti, Macroscopic and microscopic behavior of narrow elastic ribbons, Journal of Elasticity 135 (1) (2019) 409–433.

[27] J. Cui, Y. S. Chu, O. O. Famodu, Y. Furuya, J. Hattrick-Simpers, R. D. James, A. Ludwig, S. Thienhaus, M. Wuttig, Z. Zhang, I. Takeuchi, Combinatorial search of thermoelastic shape-memory alloys with extremely small hysteresis width, Nature Materials 5 (2006) 286–290.

[28] Z. Zhang, R. D. James, S. Müller, Energy barriers and hysteresis in martensitic phase transformations, Acta Materialia 57 (15) (2009) 4332–4352.

[29] Y. Song, X. Chen, V. Dabade, T. W. Shield, R. D. James, Enhanced reversibility and unusual microstructure of a phase-transforming material, Nature 502 (15) (2013) 85–88.

[30] J. G. Ratcliffe, M. W. Czabaj, T. K. O'Brien, Characterizing Delamination Migration in Carbon/Epoxy Tape Laminates, in: 27th American Society for Composites Technical Conference, Arlington, TX, 2012.